

Estimating chromophore distributions from multiwavelength photoacoustic images

B. T. Cox,^{1,*} S. R. Arridge,² and P. C. Beard¹

¹*Department of Medical Physics and Bioengineering, University College London, London WC1E 6BT, UK*

²*Department of Computer Science, University College London, London WC1E 6BT, UK*

*Corresponding author: bencox@mpb.ucl.ac.uk

Received October 15, 2008; accepted December 11, 2008;
posted December 15, 2008 (Doc. ID 102741); published January 30, 2009

Biomedical photoacoustic tomography (PAT) can provide qualitative images of biomedical soft tissue with high spatial resolution. However, whether it is possible to give accurate quantitative estimates of the spatially varying concentrations of the sources of photoacoustic contrast—endogenous or exogenous chromophores—remains an open question. Even if the chromophores' absorption spectra are known, the problem is nonlinear and ill-posed. We describe a framework for obtaining such quantitative estimates. When the optical scattering distribution is known, adjoint and gradient-based optimization techniques can be used to recover the concentration distributions of the individual chromophores that contribute to the overall tissue absorption. When the scattering distribution is unknown, prior knowledge of the wavelength dependence of the scattering is shown to be sufficient to overcome the absorption-scattering nonuniqueness and allow both distributions of chromophore concentrations and scattering to be recovered from multiwavelength photoacoustic images. © 2009 Optical Society of America

OCIS codes: 170.5120, 100.3190.

1. INTRODUCTION

The biomedical imaging modality photoacoustic tomography (PAT) has been developed over the past decade and shown to be able to provide images of soft biological tissue with high spatial resolution ($<100\ \mu\text{m}$ resolution at 5–10 mm depth) [1–5]. For contrast, it depends on the distribution of optical absorption in the imaged tissue, which in turn depends on the abundance and location of chromophores (light-absorbing molecules) within the tissue. The chromophores may be endogenous, such as hemoglobin or melanin, or exogenous, such as dyes or nanoparticles that are introduced as contrast agents.

Because of the close relationship between the photoacoustic image and the tissue optical properties, much current research in PAT is concerned with the idea that spectroscopic methods could be applied to sets of photoacoustic images obtained at multiple optical wavelengths to extract the distributions of the chromophore concentrations [6–8]. The prospect of being able to obtain accurate, quantitative, *in vivo* images of the distributions of endogenous chromophores and tagged molecular markers to sub-mm resolution with nonionizing radiation is very enticing. However, extracting chromophore concentrations from PAT images is not trivial, and there have so far been few, if any, attempts to take into account the full nonlinearity of the problem and tackle the nonunique dependence of PAT images on absorption and scattering.

Photoacoustic amplitude spectra are not, in general, directly proportional to the absorption coefficient spectra that gives rise to them. Were this the case, accurate estimates of chromophore concentration could be obtained straightforwardly by measuring photoacoustic images at a number of different wavelengths and using a simple,

linear, pixel-by-pixel spectral best-fit. As is now increasingly being recognized, the spatially varying and wavelength-dependent distribution of light within the tissue must be taken into account if accurate results are to be achieved [7,9–16]. To do so, however, is complicated by the need to estimate the nonuniform light distribution, as it will depend on the distributions of both the optical absorption and scattering coefficients of the tissue, neither of which is known in advance.

This paper investigates the inversion that maps multiwavelength photoacoustic images to chromophore distributions. The general framework involves the iterative adjustment of the optical coefficients of a numerical model of light transport until the calculated absorbed energy density at each wavelength matches the measured photoacoustic images. Two approaches to this are (1) a two-step, wavelength-by-wavelength strategy that first recovers the absorption coefficient distribution from the photoacoustic image at each wavelength and then estimates the chromophore concentrations spectroscopically from knowledge of the chromophore spectra, or (2) a one-step, all-wavelengths-at-once approach in which the chromophore concentrations are recovered using a direct inversion without the intermediate step to the absorption coefficients.

Section 2 introduces the light transport models relevant to photoacoustic imaging, and Section 3 describes iterative algorithms based on these light models that are capable of separating chromophore distributions when the optical scattering distribution is known (wavelength-by-wavelength strategies). An adjoint model is introduced that can be used for very efficient calculation of the functional gradients [9,10]. Section 4 tackles the more general

case, when the scattering coefficient distribution is unknown and potentially nonuniform, using an all-wavelengths-at-once approach. In this case, the inversion is ill-posed both because of the diffusive nature of light transport and, more severely, because of the “photoacoustic absorption-scattering nonuniqueness,” an example of which is given in Subsection 4.A. Section 4 describes and demonstrates that this nonuniqueness can be overcome using prior information about the wavelength dependence of the scattering within [17]. The singular-value decomposition (SVD) of the Hessian matrix is used to demonstrate that the nonuniqueness has been removed, and a numerical example is given in which a chromophore distribution is recovered simultaneously with the unknown scattering distribution using Newton’s method.

2. LIGHT PROPAGATION IN SCATTERING MEDIA

In a wavelength-by-wavelength inversion strategy, the first step is to extract optical absorption coefficients from photoacoustic images, and the second is to use knowledge of the chromophore absorption spectra in a spectroscopic inversion for chromophore concentrations. To see how it might be possible to extract optical absorption (and scattering) coefficients from a photoacoustic image, it is first necessary to understand how a photoacoustic image depends on them. This section therefore briefly describes the optical part of the photoacoustic forward problem: light propagation and absorption. (The second part of the forward problem, the propagation and detection of the acoustic waves, is not covered here, but details can be found in the literature [4,18].)

A. Absorbed Energy Density: Photoacoustic Image

In PAT, a short pulse of light, typically of nanoseconds duration, illuminates a region of soft tissue. The light is scattered and absorbed within the tissue, and can be described by a fluence rate $\Phi(x, t)$ in W/cm^2 , where $x \in \Omega$ is a point in the tissue and t is the time. For the examples given in this paper $\Omega \subset \mathbb{R}^2$, but similar behavior is expected in \mathbb{R}^3 ; see Section 5. The photons that are not scattered back out of the tissue are eventually absorbed by it, and when the dominant de-excitation pathway of the excited chromophores is via vibrational relaxation, the optical energy is converted to heat. The absorbed power density, the rate at which the light energy is absorbed and therefore the rate at which the tissue is locally heated, is $\mu_a \Phi$ in W/cm^3 , where $\mu_a(x)$ is the optical absorption coefficient of the tissue.

The absorbed optical energy, or equivalently the deposited heat energy, causes a temperature and pressure rise within the tissue local to where the absorption took place. As soft tissue is an elastic medium, this local pressure rise propagates as an acoustic (ultrasonic) wave. Because the optical propagation, absorption, and conversion to heat typically occur on a timescale much shorter than the mechanical relaxation—i.e., the local tissue mass density does not change significantly until all the optical energy has been converted to heat—it is often assumed therefore that, from the acoustic point of view, the heating occurs instantaneously. Under this assumption, the acoustic

propagation can be modeled as an initial value problem, and the temporal variation of the fluence rate Φ is not directly relevant; the key quantity is its integral over time, the fluence, $\phi(x) = \int \Phi(x, t) dt$ in J/cm^2 . The total amount of optical energy deposited over the duration of the pulse, the absorbed energy density, \mathcal{H} in J/cm^3 , is then given by

$$\mathcal{H}(x, t) = \mu_a(x) \phi(x) \delta(t) = h(x) \delta(t), \quad (1)$$

where the spatial part of \mathcal{H} is written as $h(x) = \mu_a(x) \phi(x)$. Thermodynamic considerations [19] lead to the following expressions for the spatially varying temperature and pressure rises T_0 and p_0 , respectively, due to the energy deposited at time $t=0$:

$$T_0 = h/(\rho C_v), \quad p_0 = (\beta v_s^2/C_p)h = \Gamma h. \quad (2)$$

Here ρ is the mass density, C_v and C_p are the specific heat capacities at constant volume and pressure, β is the linear thermal expansivity, and v_s is the sound speed. Γ , the conversion factor between absorbed optical energy density and acoustic pressure, is called the Grüneisen parameter and is dimensionless.

The aim in photoacoustic image reconstruction is to estimate the initial pressure distribution p_0 accurately from measurements of the propagating acoustic pressure waves over a measurement surface surrounding p_0 . Several exact and approximate algorithms have been proposed to solve this acoustic inversion [4,20]. As the focus of this paper is on recovering optical coefficients from photoacoustic images, and not on the reconstruction of the images themselves, it will be assumed that p_0 has already been recovered accurately. It will also be assumed that the Grüneisen coefficient Γ is known, so that the photoacoustic images can be scaled to be images of the absorbed energy density $h = p_0/\Gamma$. The relationship between a photoacoustic image h and the optical absorption and reduced scattering coefficients μ_a and μ'_s , respectively, can therefore be written as

$$h = \mu_a \phi(\mu_a, \mu'_s). \quad (3)$$

This is the fundamental equation regarding the relationship between the photoacoustic image and the optical coefficients. With the dependence on spatial position and wavelength x and λ shown explicitly, Eq. (3) is

$$h(x, \lambda) = \mu_a(x, \lambda) \phi[x, \lambda, \mu_a(x, \lambda), \mu'_s(x, \lambda)]. \quad (4)$$

B. Optical Absorption and Scattering

The optical absorption of tissue arises from the optical absorption of its constituent molecules (potentially including naturally occurring chromophores, contrast agents, and biomolecular probes). For some wavelength ranges, only a few chromophores dominate the absorption. For example, in the near-infrared the absorption is predominantly due to oxy- and deoxy-haemoglobin, water, and lipids [7]. If the concentrations of the K significant chromophores are written as $c_k(x)$, $k=1, \dots, K$, then the absorption coefficient (over a given wavelength range) may be written as the sum

$$\mu_a(x, \lambda) = \sum_{k=1}^K c_k(x) \alpha_k(\lambda), \quad (5)$$

where $\alpha_k(\lambda)$ are the specific absorption coefficient spectra of the chromophores [7,21]. The main topic of this paper is the inversion of Eqs. (4) and (5) to obtain the chromophore concentrations $c_k(x)$ from the multiwavelength images $h(x, \lambda)$ when the spectra $\alpha_k(\lambda)$ are known.

The scattering in highly scattering media such as biological tissue can be described by the scattering coefficient $\mu_s(x, \lambda)$, or equivalently the reduced scattering coefficient $\mu'_s = \mu_s(1-g)$ where g is a parameter that accounts for some anisotropy in the scattering [22]. The wavelength dependence of μ'_s has been measured for many types of tissue and can often be approximated by

$$\mu'_s(x, \lambda) \approx a(x)\lambda^{-b}, \quad (6)$$

where the constant $b > 0$ is known from experiment [23–25]. Prior knowledge of the exponent b will be used in the multiwavelength inversion in Section 4 to overcome the absorption-scattering nonuniqueness described in Subsection 4.A.

C. Light Transport Models

In order to study the inversion of Eq. (4), it is necessary to choose a form or a model to describe the light fluence distribution $\phi(x)$. Light propagation in a scattering medium is often modeled using the random walk approach of Monte Carlo simulations [26,27], which is widely considered the most accurate technique, but is computationally inefficient as the paths of many millions of photons must be calculated to obtain a good estimate of the fluence. This inefficiency makes it an unsuitable candidate for iterative inversions in which the fluence must be calculated numerous times.

Alternative models are usually based on Boltzmann's transport equation (sometimes called the radiative transfer equation) in which the tissue is characterized by the absorption and scattering coefficients μ_a and μ_s and a "phase function" that describes the directionality of the scattering process [22]. This integrodifferential equation in the *radiance*—a description of the light as a time-varying function of direction at every point—expresses the conservation of energy during the scattering and absorption processes. Because it is difficult to solve analytically, in practice approximations are used and in all but the simplest cases are solved numerically [22,28,29]. Some approximations, including the diffusion approximation used in this paper, have the additional advantage that the equations are simple enough to manipulate directly, which can be helpful when tackling the inverse problem, e.g., by allowing gradients to be calculated analytically rather than numerically.

The "diffusion approximation" to the radiative transfer equation has been used widely in biomedical optical imaging, particularly in diffuse optical tomography [28]. The time-independent case, relevant in this case, takes on the relatively simple form of a diffusion equation

$$(\mu_a - \nabla \cdot \kappa \nabla) \phi = q_0, \quad (7)$$

where $\kappa = [3(\mu_a + \mu'_s)]^{-1}$ is the optical diffusion coefficient, and q_0 is an isotropic source term. To obtain the diffusion equation from the radiative transport equation, the light fluence, ϕ , is assumed to be almost isotropic everywhere. Equation (7) is therefore usually considered an accurate approximation to the radiative transport equation when $\mu'_s \gg \mu_a$ [28]. However, in tissue, light is quite strongly forward scattered (typically $g \approx 0.9$), so for a nondiffuse source exterior to the domain, this model is accurate only for distances greater than a scattering length inside the boundary, $1/\mu'_s$, where the fluence has become diffuse. For this reason, a collimated beam incident on the boundary is often modeled by a point source placed one scattering length inside it [30]. This is the approach taken in this paper, using a finite-element (FE) implementation of the diffusion equation [29,30].

3. MULTIWAVELENGTH INVERSIONS FOR CHROMOPHORE CONCENTRATIONS: SCATTERING KNOWN

As stated previously, the main aim of this paper is to explore ways in which chromophore concentrations $c_k(x)$ might be recovered from photoacoustic images. This section and Section 4 describe inversion techniques for when the optical scattering is known and unknown, respectively. These cases are fundamentally different in that the latter is much more ill-posed due to the absorption-scattering nonuniqueness (Subsection 4.A), although similar optimization tools can be employed to solve both.

When the scattering coefficient distribution is known, one way to estimate the chromophore distributions is first to estimate the absorption coefficient distributions from the images of absorbed energy one wavelength at a time, $h(x, \lambda_0) \rightarrow \mu_a(x, \lambda_0)$, $h(x, \lambda_1) \rightarrow \mu_a(x, \lambda_1)$, etc, and then use these recovered absorption coefficient spectra $\mu_a(x, \lambda_i)$ in a linear inversion of Eq. (5) to estimate the chromophore distributions $c_k(x)$. An alternative approach is to minimize the difference between the measured images and those generated using a model by adjusting the chromophores, thus estimating $c_k(x)$ directly using nonlinear optimization, without first obtaining the single-wavelength absorption coefficients. Both methods are described below.

A. Fixed-Point Iterative Inversion for Absorption Coefficients

When the scattering is known, there is a simple way to estimate the absorption coefficient from a photoacoustic image [9,10]. Given the image $\hat{h}(x)$, the absorption coefficient can be recovered using the fixed-point iteration

$$\mu_a^{(n+1)}(x) = \hat{h}(x) / (\phi^{(n)}(x) + \epsilon), \quad (8)$$

where $\phi^{(n)} = \phi[\mu_a^{(n)}, \mu'_s]$ is the fluence calculated from a model of light transport using the n th estimate of the absorption coefficient, and ϵ is a regularization parameter. This approach was applied to experimental data by Yuan and Jiang [31]. If the specific absorption coefficient spectra of the chromophores within the tissue $\alpha_k(\lambda)$ are

known, then the absorption coefficient images can be mapped to chromophore distributions by inverting Eq. (5), a single matrix inversion.

B. Other Inversions for Absorption Coefficients

Banerjee *et al.* [32] have recently proposed a noniterative version similar to the fixed-point iteration above by assuming the diffusion coefficient in Eq. (7) $\kappa \approx 1/(3\mu'_s)$ (true when $\mu'_s \gg \mu_a$), which allows the fluence to be obtained directly by solving $(\nabla \cdot \kappa \nabla)\phi = \hat{h} - q_0$. Ripoll and Ntziachristos [33] also describe an inversion scheme based on the diffusion model that can recover small perturbations in the absorption coefficient distribution when both the scattering and background absorption coefficients are known. Yin *et al.* [34] suggest making additional measurements of the fluence leaving the tissue and using diffuse optical tomography (DOT) to estimate the interior fluence distribution, although this will suffer from the poor spatial resolution achievable with DOT. Yuan *et al.* [35] propose the use of *a priori* structural information as a means of regularization, where “the PAT image (absorbed energy density map) is used both as input data and as prior structural information” [35], p. 18078. The difficulty with this form of regularization is that the PAT image may not give accurate structural information as it is distorted by the non-uniform fluence. Indeed, the desire to obtain an image that is physiologically accurate structurally is one of the motivations for inverting for the optical coefficients.

The difference between two images can be used to assess changes before and after a contrast agent is introduced, or to compare two images at different wavelengths if one of the chromophores contributes negligible absorption at one of the wavelengths and the other has similar absorption at both. A “difference” or “subtraction” image can provide useful qualitative images that highlight regions where the absorption has changed [16]. However, simple considerations show that this approach is of no benefit to *quantitative* imaging. If in the first measurement there is only one absorber present μ_{a1} , but in the second there is also a second μ_{a2} , then the absorbed energy images in the two cases will be

$$h_1 = \mu_{a1}\phi_1, \quad (9)$$

$$h_2 = (\mu_{a1} + \mu_{a2})\phi_2, \quad (10)$$

where ϕ_1 and ϕ_2 are the fluence distributions in the two cases. The difference image is given by

$$h_2 - h_1 = \mu_{a1}(\phi_2 - \phi_1) + \mu_{a2}\phi_2, \quad (11)$$

which, if $\phi_2 = \phi_1$, would be the same as a photoacoustic image taken with only the second absorber present. While this may be a useful qualitative tool in cases where the change in the fluence is minimal, it does nothing to assist in our attempt to extract chromophore concentrations, as the fluence distribution is still unknown.

C. Gradient-Based Inversion for Absorption or Scattering: Adjoint Model

An alternative approach to estimating the absorption coefficient images $\mu_a(x)$ from $\hat{h}(x)$, and one which has the advantage that it can be used to estimate the scattering

coefficient if μ_a is known, is to minimize a functional quantifying the difference between the model output h and the measurements \hat{h} by adjusting $\mu_a(x)$:

$$\operatorname{argmin}_{\mu_a(x)} \mathcal{E}_{\mu_a} = \frac{1}{2} \int [h(\mu_a) - \hat{h}]^2 d\Omega. \quad (12)$$

(The $\frac{1}{2}$ is included here so that the derivatives are not cluttered by factors of 2.)

One way to find the minimum is to calculate the gradients of the functional \mathcal{E}_{μ_a} with respect to μ_a at each point and perform a directed search for the minimum. The equivalent problem for scattering is obtained by replacing μ_a with μ'_s in Eq. (12):

$$\operatorname{argmin}_{\mu'_s(x)} \mathcal{E}_{\mu'_s} = \frac{1}{2} \int [h(\mu'_s) - \hat{h}]^2 d\Omega. \quad (13)$$

The functional gradients for both problems can be found efficiently by using the adjoint equation

$$(\mu_a - \nabla \cdot \kappa \nabla)\phi^* = \mu_a(h - \hat{h}), \quad (14)$$

with adjoint solution ϕ^* . The functional gradients for the absorption and scattering can then be calculated via the equations [36]

$$\frac{\partial \mathcal{E}_{\mu_a}}{\partial \mu_a(x)} = \phi(x)[h(x) - \hat{h}(x)] - \phi^*(x)\phi(x), \quad (15)$$

$$\frac{\partial \mathcal{E}_{\mu'_s}}{\partial \mu'_s(x)} = 3\kappa(x)^2 \nabla \phi^*(x) \cdot \nabla \phi(x). \quad (16)$$

In other words, by solving Eqs. (7) and (14) just once each, the functional gradients can be calculated from Eqs. (15) and (16)—a much more efficient way to calculate the gradients than the common method of finite differences. (Note that because both the forward and adjoint equations are in the form of diffusion equations, the same numerical model can be used for both.) It has been shown that by using a gradient descent algorithm, such as the Broyden–Fletcher–Goldfarb–Shanno (BFGS) minimization routine, either the absorption or reduced scattering coefficient distributions can be recovered when the other is known in advance [36].

D. Inversion for Chromophore Concentrations

Extending the minimization approach from absorption coefficients to chromophores is straightforward. In this case the problem becomes

$$\operatorname{argmin}_{c_k(x)} \mathcal{E}_c = \frac{1}{2} \int \int [h(c_k) - \hat{h}]^2 d\Omega d\lambda, \quad (17)$$

where h and \hat{h} now represent a set of images obtained at multiple wavelengths and a second integral over wavelength is included. Using Eq. (5) the functional gradient with respect to the chromophores c_k can be calculated using

$$\frac{\partial \mathcal{E}_c}{\partial c_k} = \int \alpha_k(\lambda) \frac{\partial \mathcal{E}_{\mu_a}}{\partial \mu_a}(\lambda) d\lambda. \quad (18)$$

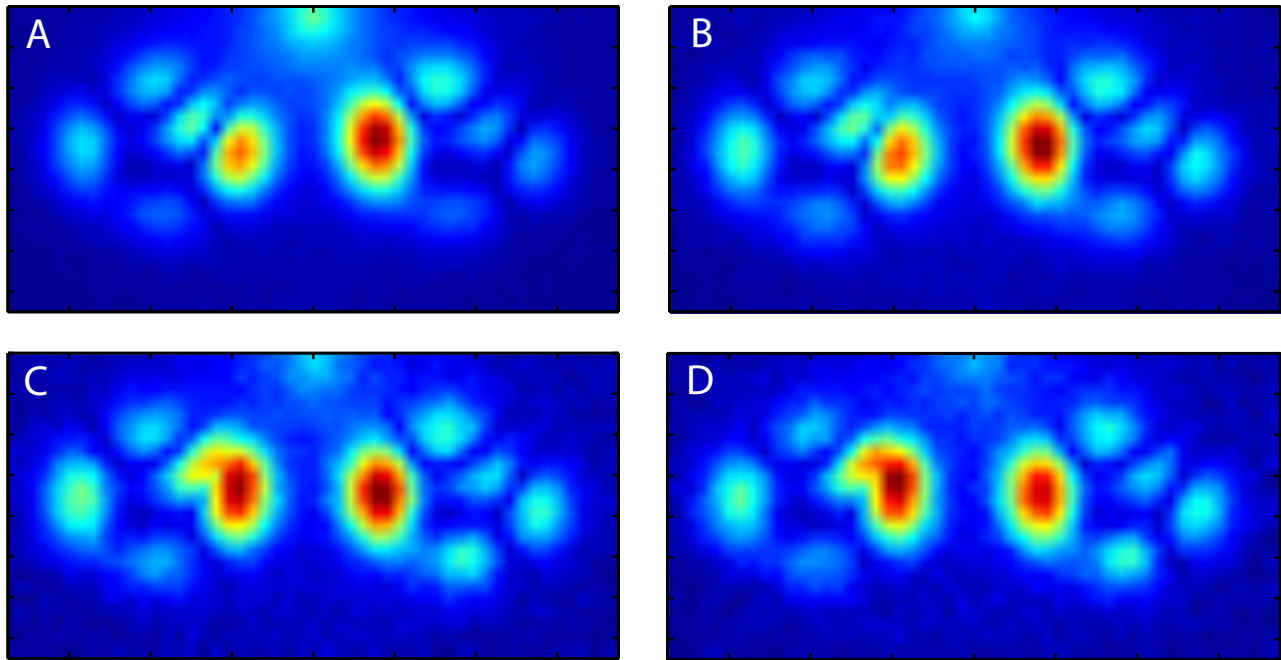


Fig. 1. (Color online) Images of absorbed optical energy density due to two chromophores with different absorption spectra, shown at four wavelengths: (A) 650, (B) 750, (C) 850, (D) 950 nm. The image dimensions are $3.75 \text{ mm} \times 8 \text{ mm}$, a point source is positioned 0.25 mm beneath the upper surface, and the anisotropy factor is 0.9. Each image is normalized by its maximum value to optimize the visible dynamic range.

In the following example, the absorbed energy density at four wavelengths (650, 750, 850, and 950 nm) was calculated assuming that only two chromophores contribute to the absorption. The reduced scattering coefficient μ'_s was set constant at 2 mm^{-1} . A point source of light was positioned 0.25 mm below the boundary; see Fig. 1. The two chromophores were chosen to have absorption spectra similar to deoxyhemoglobin and oxyhemoglobin; see Fig. 2. Their concentrations, $c_1(x)$ and $c_2(x)$, respectively, are shown in Figs. 3A and 3B.

In the simulated photoacoustic images shown in Fig. 1, it is immediately apparent that it is not possible to see the patterns of both underlying chromophore distributions from these plots. However, the least-squares minimization, Eq. (17), can recover the two separate chromophore distributions accurately. The estimates after 500 iterations are shown in Figs. 3C, 3D, and 4. The adjoint model,

Eq. (14), provided the functional gradients, and the BFGS routine as encoded in Matlab's `fminunc` function was used to perform the minimization.

4. MULTIWAVELENGTH INVERSION FOR CHROMOPHORE CONCENTRATIONS: SCATTERING UNKNOWN

The assumption in Section 3 was that the optical scattering was known. In some situations it may be possible to estimate the scattering coefficient accurately, for instance, in tissues that are fairly homogeneous. In general, though, this will not be the case, and the photoacoustic absorption-scattering nonuniqueness makes the inversion for the chromophore concentrations ill-posed. An example of this nonuniqueness is given in Subsection 4.A. In the remainder of this section, the notation and framework for tackling the inversion using a well-known nonlinear optimization (Newton's method) will be given, and an example will be used to show that prior knowledge of the wavelength dependence of the scattering, exponent b in Eq. (6), is sufficient to remove the nonuniqueness.

A. Absorption-Scattering Nonuniqueness

While the gradient-based approach described in Section 3 has the two advantages that (a) the gradients can be calculated efficiently using the adjoint model, and (b) it can recover either the absorption or scattering coefficient distributions when the other is known, there remains a difficulty when trying to recover both absorption and scattering coefficient distributions together. Given a measurement of the absorbed energy density $\hat{h}(x)$ at a single wavelength, it is not possible in general to recover absorption and scattering distributions *simultaneously*

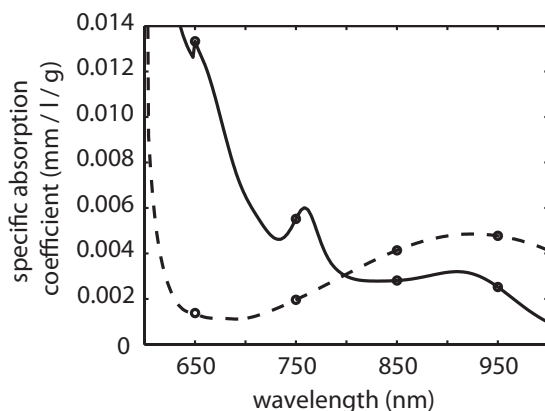


Fig. 2. Specific absorption coefficients (mm/l/g) of oxyhemoglobin and deoxyhemoglobin, the two chromophores whose concentrations are shown in Figs. 3A and 3B.

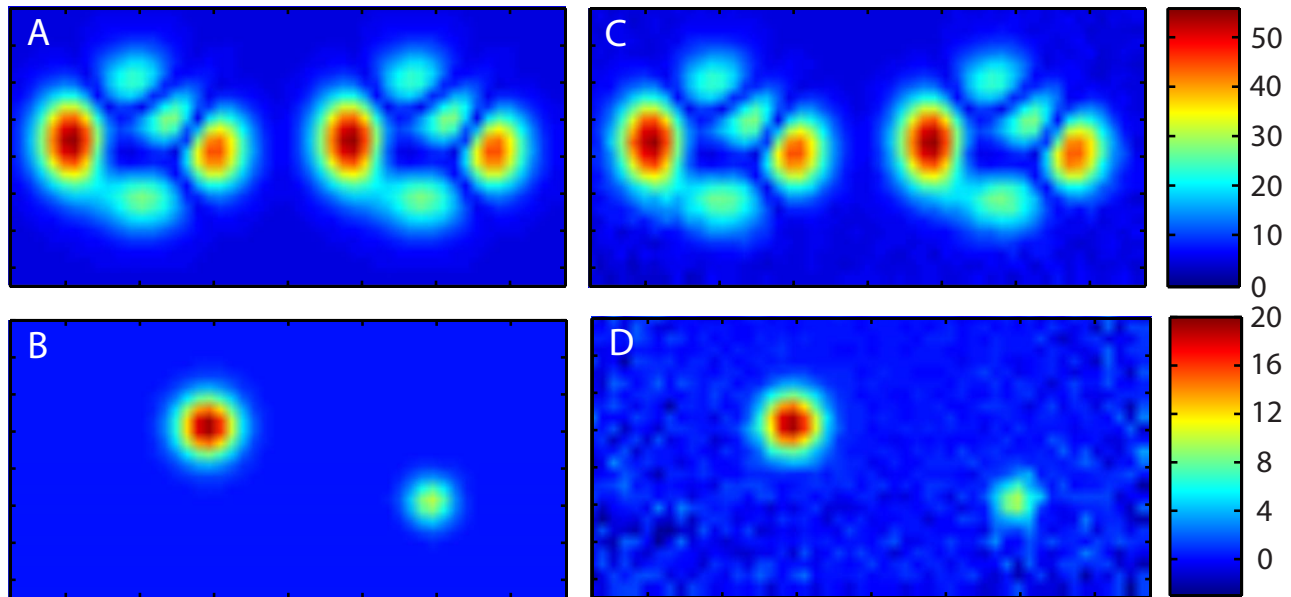


Fig. 3. (Color online) True concentration distributions (g/l) of two chromophores (images A and B) and their estimates (images C and D) successfully obtained by minimizing Eq. (17) using a gradient-based algorithm (BFGS) with the multiwavelength absorbed energy images from Fig. 1 as input data. The functional gradients were calculated efficiently using an adjoint model, and the scattering was known *a priori*. The image dimensions are 3.75 mm \times 8 mm.

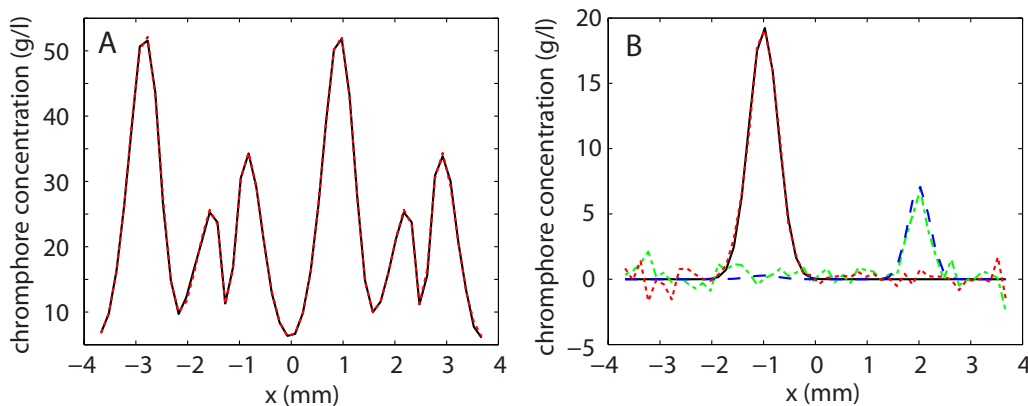


Fig. 4. (Color online) Profiles through the chromophore concentrations (g/l) shown in Fig. 3. (A) Exact (solid) and estimated (dotted) profiles at 1.6 mm through Figs. 3A and 3C, respectively. (B) Profiles at 1.6 mm, exact (solid) and estimated (dotted), and at 2.3 mm, exact (dashed), estimated (dotted-dashed) through Figs. 3B and 3D, respectively.

and *uniquely*. The reason is that both the absorption and the scattering can affect the fluence distribution, and so when the calculated absorbed energy $h(x)$ differs from the measured absorbed energy $\hat{h}(x)$ it is not possible to say whether this is due to an error in the absorption coefficient distribution or in the scattering coefficient distribution.

A numerical example of this nonuniqueness will help to clarify the difficulty it poses. By using a FE implementation of the diffusion model of light transport described in Subsection 2.C, the absorption and scattering coefficient distributions shown in Fig. 5A and 5B, μ_{a1} and μ_{s1} , were calculated to give rise to the absorbed energy distribution h_1 shown in Fig. 5C. (The model was encoded in Matlab on a 25×50 mesh representing a 4 mm \times 8 mm rectangle, a point source was placed 0.25 mm inside the upper boundary, and the boundary condition set such that the incoming photon current is zero.) The scattering coefficient

was then set to the distribution shown in Fig. 5E, μ_{s2} , and a gradient-based minimization [with the Matlab routine `fminunc` using the BFGS algorithm, and the gradients calculated from Eq. (15)] was used to find the absorption coefficient μ_{a2} that would minimize the functional $\mathcal{E}_{nonunique}$

$$\mathcal{E}_{nonunique} = \frac{1}{2} \int [h_2(\mu_{a2}, \mu_{s2}) - h_1(\mu_{a1}, \mu_{s1})]^2 d\Omega. \quad (19)$$

Fig. 5D shows μ_{a2} when the differences between h_2 and h_1 were negligible. h_2 is shown in Fig. 5F and the differences $\mu_{a1} - \mu_{a2}$, $\mu_{s1} - \mu_{s2}$, and $h_1 - h_2$ are shown in Figs. 5G, 5H, and 5J, respectively. The two pairs (μ_{a1}, μ_{s1}) and (μ_{a2}, μ_{s2}) are an example of the absorption-scattering nonuniqueness, in the sense that both result in the same absorbed energy distribution. A standard response to a nonuniqueness in an inverse problem like this is to try and incorpo-

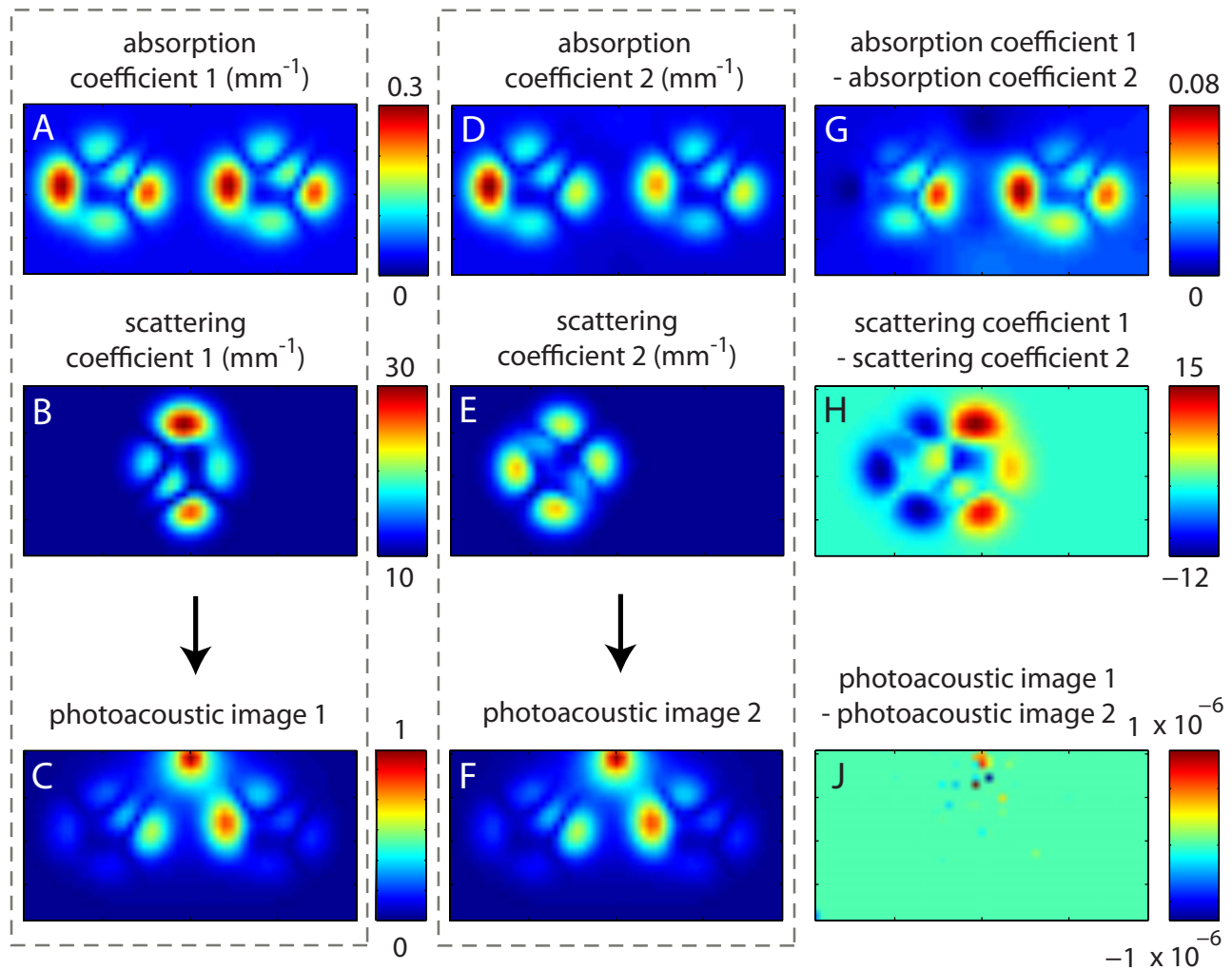


Fig. 5. (Color online) Optical absorption-scattering nonuniqueness. The absorption and scattering coefficient distributions A and B give rise to the absorbed energy distribution (to which the photoacoustic image is proportional) shown in C. The absorption and scattering distributions D and E also give rise to the same absorbed energy distribution, which is shown in F. The differences between the absorption, scattering, and absorbed energy images are shown on the right in G, H, and J, respectively. The fact that these absorbed energy densities are indistinguishable (J is virtually zero everywhere) demonstrates the nonuniqueness of the relationship between a single-wavelength photoacoustic image and the underlying optical coefficients. The image dimensions are $4 \text{ mm} \times 8 \text{ mm}$, a point source is positioned 0.25 mm beneath the upper surface, and the anisotropy factor is 0.9 .

rate some additional information, such as prior knowledge of the type of solution, into the problem to reduce the size of the solution space. Unfortunately, simple constraints on the smoothness of the coefficient distributions—such as may be provided by Tikhonov-style regularization—will not be sufficient in this case. Indeed, from this example it is clear that both sets of optical parameters have similar degrees of smoothness, and it will not be possible to separate them on that basis. However, the problem posed by the nonuniqueness can be overcome, in the sense that the chromophores can be recovered by using prior knowledge of the wavelength dependence of the scattering as described below [17,21].

B. Error Functional and Sensitivity Equations

The unknown quantities from now on are the spatial distributions of the concentrations of the K chromophores $c_k(x)$ and the spatial dependence of the scattering $a(x)$, rather than the absorption and scattering coefficient dis-

tributions $\mu_a(x)$ and $\mu'_s(x)$. The problem is similar to Eq. (17), except the scattering amplitude $a(x)$ is also unknown:

$$\operatorname{argmin}_{c_k(x), a(x)} \mathcal{E} = \frac{1}{2} \iint [h(c_k, a) - \hat{h}]^2 d\Omega d\lambda. \quad (20)$$

The sensitivity of \mathcal{E} to changes in c_k and a guide the minimization by indicating the local shape of the error functional. Differentiating Eq. (20) with respect to c_k and a gives

$$\frac{\partial \mathcal{E}}{\partial c_k} = \iint \frac{\partial h}{\partial c_k} [h(c_k, a) - \hat{h}] d\Omega d\lambda, \quad (21)$$

$$\frac{\partial \mathcal{E}}{\partial a} = \iint \frac{\partial h}{\partial a} [h(c_k, a) - \hat{h}] d\Omega d\lambda. \quad (22)$$

The derivatives $\partial h / \partial c_k$ and $\partial h / \partial a$ are related to $\partial h / \partial \mu_a$ and $\partial h / \partial \mu'_s$, respectively, by

$$\frac{\partial h}{\partial c_k} = \alpha_k \frac{\partial h}{\partial \mu_a}, \quad (23)$$

$$\frac{\partial h}{\partial a} = \lambda^{-b} \frac{\partial h}{\partial \mu_s'}, \quad (24)$$

and $\partial h / \partial \mu_a$ and $\partial h / \partial \mu_s'$ may be calculated from

$$\frac{\partial h(x)}{\partial \mu_a(x')} = \phi(x) \delta(x - x') + \mu_a(x) \frac{\partial \phi(x)}{\partial \mu_a(x')}, \quad (25)$$

$$\frac{\partial h(x)}{\partial \mu_s'(x')} = \mu_a(x) \frac{\partial \phi(x)}{\partial \mu_s'(x')}, \quad (26)$$

which come from differentiating Eq. (3). Equations for $\partial \phi / \partial \mu_a$ and $\partial \phi / \partial \mu_s'$, the sensitivity of fluence with respect to the optical parameters, may in turn be derived from Eq. (7). The sensitivity of the fluence $\phi(x)$ at point x to a change in the absorption coefficient $\mu_a(x')$ at point x' may be calculated from

$$(\mu_a - \nabla \cdot \kappa \nabla) \frac{\partial \phi(x)}{\partial \mu_a(x')} = -\phi(x) \delta(x - x'). \quad (27)$$

Similarly for the diffusion coefficient κ

$$(\mu_a - \nabla \cdot \kappa \nabla) \frac{\partial \phi(x)}{\partial \kappa(x')} = \nabla \cdot [\delta(x - x') \nabla \phi(x)]. \quad (28)$$

The reduced scattering coefficient and the diffusion coefficient are related by $\kappa = [3(\mu_a + \mu_s')]^{-1}$, so differentiating gives the sensitivity relation $\partial \kappa / \partial \mu_s' = -3\kappa^2$. All the gradients and sensitivities required for a minimization could be calculated from these equations. However, as the light model was encoded using a FE model, the gradients could also be obtained by differentiating the basis functions directly. This avoids the numerical difficulties posed by the discretization of terms such as $\nabla \cdot [\delta(x - x') \nabla \phi(x)]$.

C. Discrete Notation

Images are not continuous functions of x but discretized, so it is helpful to have a notation to describe the discrete case. For the remainder of this paper, the coordinates of the pixels (or voxels) of the photoacoustic image of h will be denoted by x_m , $m = 1, \dots, M$, and the optical coefficients or chromophores will be defined at points x_n , $n = 1, \dots, N$. (The meshes defined by these points may of course be the same.) Also, the subscripts k and l will be used to indicate the different chromophores and wavelengths, respectively. The following column vectors will be useful:

- the absorbed energy distribution at wavelength λ_l , $\mathbf{h}^{\lambda_l} = (h_1^{\lambda_l}, \dots, h_M^{\lambda_l})^T = [h(x_1, \lambda_l), \dots, h(x_M, \lambda_l)]^T$,
- the concentration distribution of chromophore k , $\mathbf{c}_k = (c_{k1}, \dots, c_{kN})^T = [c_k(x_1), \dots, c_k(x_N)]^T$,
- and the spatial variation of the scattering, $\mathbf{a} = (a_1, \dots, a_N)^T = [a(x_1), \dots, a(x_N)]^T$.

For the multiwavelength inversions, these column vectors are concatenated into long, multiwavelength column vectors:

$$\mathbf{h} = \begin{pmatrix} \mathbf{h}^{\lambda_1} \\ \vdots \\ \mathbf{h}^{\lambda_L} \end{pmatrix} = \begin{pmatrix} h_1^{\lambda_1} \\ \vdots \\ h_M^{\lambda_1} \\ \vdots \\ h_1^{\lambda_L} \\ \vdots \\ h_M^{\lambda_L} \end{pmatrix}, \quad \mathbf{c} = \begin{pmatrix} \mathbf{c}_1 \\ \vdots \\ \mathbf{c}_K \end{pmatrix} = \begin{pmatrix} c_{11} \\ \vdots \\ c_{1N} \\ \vdots \\ c_{K1} \\ \vdots \\ c_{KN} \end{pmatrix}.$$

D. Gradient, Hessian, and Jacobian

With continuous variables, the problem was to find the distributions $c_k(x)$ and $a(x)$ that minimized the error functional in Eq. (20) given the continuous measured data \hat{h} . In the discrete case, the problem is still to find the chromophore concentrations and scattering that minimize an error functional, but they are no longer continuous functions but finite-length vectors \mathbf{c} and \mathbf{a} . For succinctness, they will be combined together into a single vector of unknowns:

$$\mathbf{u} = \begin{pmatrix} \mathbf{c} \\ \mathbf{a} \end{pmatrix}. \quad (29)$$

The error functional \mathcal{E} is no longer defined as an integral but as a sum over image pixels and wavelengths,

$$\mathcal{E}(\mathbf{u}) = \frac{1}{2} \sum_{l=1}^L \sum_{m=1}^M [h_m^{\lambda_l}(\mathbf{u}) - \hat{h}_m^{\lambda_l}]^2 = \frac{1}{2} \mathbf{e}^T \mathbf{e}, \quad (30)$$

where $\mathbf{e} = \mathbf{h} - \hat{\mathbf{h}}$ is the vector of residuals. From now on \mathcal{E} will be used to refer to this discrete version of the error functional.

One way to search for the minimum of \mathcal{E} is to use the iterative inversion scheme known as Newton's method [37]. A brief description of it is given here for completeness. First note that \mathcal{E} is a continuous function of the unknown parameter vector \mathbf{u} , and so its Taylor expansion about \mathbf{u}_0 exists as

$$\mathcal{E}(\mathbf{u}_0 + \boldsymbol{\delta}) \approx \mathcal{E}(\mathbf{u}_0) + \mathbf{g}^T \boldsymbol{\delta} + \frac{1}{2} \boldsymbol{\delta}^T \mathbf{H} \boldsymbol{\delta} + \dots, \quad (31)$$

where $\boldsymbol{\delta}$ represents a perturbation to the unknowns \mathbf{u}_0 . The first-order derivative vector \mathbf{g} and second-order derivative matrix \mathbf{H} are called the (functional) gradient and Hessian, respectively. Differentiating the Taylor series in Eq. (31) and setting it to zero gives $\mathbf{g} = -\mathbf{H} \boldsymbol{\delta}$, which can be rearranged into an expression for an "update" vector

$$\boldsymbol{\delta} = -\mathbf{H}^{-1} \mathbf{g} \approx -(\mathbf{J}^T \mathbf{J})^{-1} \mathbf{J} \mathbf{e}. \quad (32)$$

At each step, the latest estimate of \mathbf{u} is updated, $\mathbf{u} \leftarrow \mathbf{u} + \boldsymbol{\delta}$, until the value of \mathbf{u} that minimizes \mathcal{E} , or a good approximation to it, is reached. The gradient vector \mathbf{g} and Hessian matrix \mathbf{H} are given by

$$\mathbf{g} = \left[\frac{\partial \mathcal{E}}{\partial c_{11}}, \dots, \frac{\partial \mathcal{E}}{\partial c_{KN}}, \frac{\partial \mathcal{E}}{\partial a_1}, \dots, \frac{\partial \mathcal{E}}{\partial a_N} \right]^T, \quad (33)$$

$$H = \left[\begin{array}{cc|cc} \frac{\partial^2 \mathcal{E}}{\partial c_{11}^2} & \dots & \frac{\partial^2 \mathcal{E}}{\partial c_{11} \partial c_{KN}} & \frac{\partial^2 \mathcal{E}}{\partial c_{11} \partial a_1} & \dots & \frac{\partial^2 \mathcal{E}}{\partial c_{11} \partial a_N} \\ \vdots & \ddots & \vdots & \vdots & \ddots & \vdots \\ \frac{\partial^2 \mathcal{E}}{\partial c_{KN} \partial c_{11}} & \dots & \frac{\partial^2 \mathcal{E}}{\partial c_{KN}^2} & \frac{\partial^2 \mathcal{E}}{\partial c_{KN} \partial a_1} & \dots & \frac{\partial^2 \mathcal{E}}{\partial c_{KN} \partial a_N} \\ \hline \frac{\partial^2 \mathcal{E}}{\partial a_1 \partial c_{11}} & \dots & \frac{\partial^2 \mathcal{E}}{\partial a_1 \partial c_{KN}} & \frac{\partial^2 \mathcal{E}}{\partial a_1^2} & \dots & \frac{\partial^2 \mathcal{E}}{\partial a_1 \partial a_N} \\ \vdots & \ddots & \vdots & \vdots & \ddots & \vdots \\ \frac{\partial^2 \mathcal{E}}{\partial a_N \partial c_{11}} & \dots & \frac{\partial^2 \mathcal{E}}{\partial a_N \partial c_{KN}} & \frac{\partial^2 \mathcal{E}}{\partial a_N \partial a_1} & \dots & \frac{\partial^2 \mathcal{E}}{\partial a_N^2} \end{array} \right] \quad (34)$$

Note that the gradient, unlike the Hessian, depends on the measured data \hat{h} . Both the Hessian and gradient can be calculated from the Jacobian matrix, as $H \approx \mathbf{J}^T \mathbf{J}$ and $\mathbf{g} = \mathbf{J}^T \mathbf{e}$, although the gradient can be calculated more efficiently using the adjoint model described in Subsection 3.C. The elements of the Jacobian matrix are the sensitivities of the model output h to changes in the unknowns. For instance, the Jacobian matrices for \mathbf{c} and \mathbf{a} at wavelength λ_l are

$$\mathbf{J}_c^{\lambda_l} = \begin{bmatrix} \frac{\partial h_1^{\lambda_l}}{\partial c_1} & \dots & \frac{\partial h_1^{\lambda_l}}{\partial c_{KN}} \\ \vdots & \ddots & \vdots \\ \frac{\partial h_M^{\lambda_l}}{\partial c_1} & \dots & \frac{\partial h_M^{\lambda_l}}{\partial c_{KN}} \end{bmatrix}, \quad (35)$$

$$\mathbf{J}_a^{\lambda_l} = \begin{bmatrix} \frac{\partial h_1^{\lambda_l}}{\partial a_1} & \dots & \frac{\partial h_1^{\lambda_l}}{\partial a_N} \\ \vdots & \ddots & \vdots \\ \frac{\partial h_M^{\lambda_l}}{\partial a_1} & \dots & \frac{\partial h_M^{\lambda_l}}{\partial a_N} \end{bmatrix}. \quad (36)$$

The elements of the single-wavelength Jacobians can be calculated column by column using Eqs. (23)–(28), and the multiwavelength Jacobian matrix can then be constructed as

$$\mathbf{J} = \left[\begin{array}{c|c} \mathbf{J}_c^{\lambda_1} & \mathbf{J}_a^{\lambda_1} \\ \mathbf{J}_c^{\lambda_2} & \mathbf{J}_a^{\lambda_2} \\ \vdots & \vdots \\ \mathbf{J}_c^{\lambda_L} & \mathbf{J}_a^{\lambda_L} \end{array} \right]. \quad (37)$$

This potentially huge multiwavelength Jacobian does not necessarily need to be stored in full, because the multiwavelength Hessian and gradient could be calculated as the sum of single-wavelength Hessians and gradients.

E. Example

A proof-of-principle numerical example will be used to demonstrate that the absorption-scattering nonuniqueness is not a problem for multiwavelength chromophore inversions when using prior knowledge of the dependence of the scattering on wavelength. Figures 8A and 8B below show the spatial distributions of a single chromophore concentration $c(x)$ and the spatial part of the scattering coefficient $a(x)$, respectively. A small 25×50 mesh representing $3.6 \text{ mm} \times 7.5 \text{ mm}$ was deliberately chosen to keep the size of the inversion reasonable. Even with this small example consisting of only two unknown parameter distributions, the number of unknowns is 2500, the Hessian matrix has $2500^2 = 6.25 \times 10^6$ elements and the multiwavelength Jacobian $5000 \times 2500 = 12.5 \times 10^6$ elements. (The large scale of this type of inversion is discussed further in Section 5 below.)

The FE model of light transport described above was used both to simulate the “measured” data \hat{h} and as the forward model in the inversion scheme. To mitigate this “inverse crime” the former was calculated on and linearly interpolated from a larger, noncoincident mesh, and Gaussian noise was added to give a mean signal-to-noise ratio in the “measured” images of ≈ 30 dB. The wavelength dependence of the chromophore was chosen to be similar to that of oxyhemoglobin, and the scattering wavelength dependence was set to $b = 1.3$, see Fig. 6.

The ranges of the resulting absorption and reduced scattering coefficients are shown in Table 1 as a function of wavelength. (A scaling factor was introduced to the scattering, $\mu'_s(x) = a(x)a_0\lambda^{-b} \text{ mm}^{-1}$, where $a_0 = 500$, so that the unknowns $c(x)$ and $a(x)$ were of similar magnitude.) These coefficients were chosen to be sufficiently small to demonstrate clearly the principle that the scattering-absorption nonuniqueness could be overcome using multiwavelength data. When the absorption or scattering coefficient is large, the fluence may be small at some points in the image, resulting in a low signal-to-noise ratio there. The practical question of the range of signal-to-noise ratios for which this inversion is achievable in practice is not tackled directly in this paper.

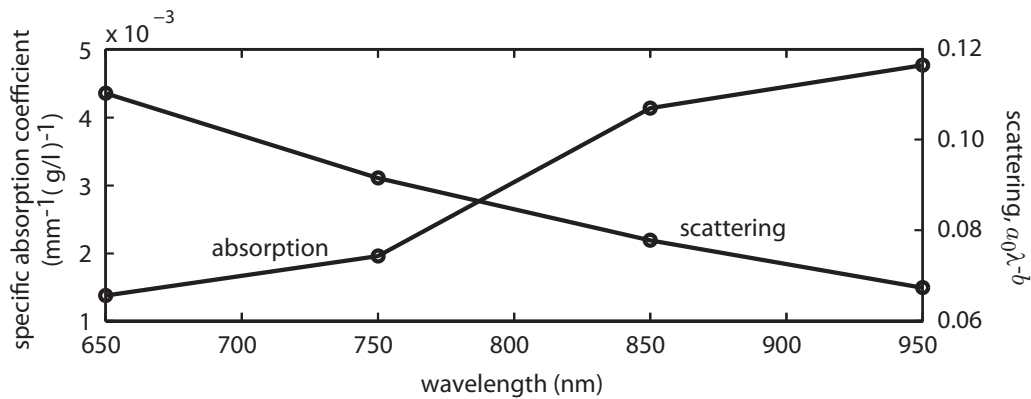


Fig. 6. Wavelength dependence of the chromophore absorption and scattering used in the example in Subsection 4.E.

F. Ill-Conditioning and Regularization

A solution for the update δ in the matrix Eq. (32) will strictly exist only when the Hessian, or its approximation $J^T J$, has an inverse. However, the existence of the inverse is not sufficient to ensure that the updates δ calculated from it are stable, in the sense that a small perturbation in the measured data leads to a small perturbation in the update δ . This will be the case only if the condition number of the Hessian is not too large. The conditioning of the Hessian can be obtained, for small problems such as the example here, by calculating the SVD $H=U\Sigma V^T$, where the columns of the full matrices U and V contain the “left” and “right” singular vectors u_i and v_i , and Σ is a diagonal matrix containing the corresponding singular values, $\sigma_1, \sigma_2, \dots$. The singular values in Σ appear in order from the largest at the top to the smallest at the bottom, and the condition number is the ratio of the largest to the smallest [38]. Substituting the SVD representation of H into Eq. (32) gives a way to calculate the update [39]

$$\delta = -V\Sigma^{-1}U^T \mathbf{g} = -\sum_i \frac{u_i^T \mathbf{g}}{\sigma_i} v_i. \quad (38)$$

From this it is clear that if the smallest singular values are very small then their reciprocals will be very large and will make the solution overly sensitive to noise in the data. Measures taken to prevent this are generically termed regularization. Two popular ways are the truncated-SVD, in which the sum over i in Eq. (38) is truncated to include only some of the singular values and vectors in the reconstructed image, and Tikhonov, in which a filter $\sigma_i^2/(\sigma_i^2 + \epsilon^2)$ is used to weight the inverted singular values. ϵ is a variable regularization parameter. The value of i at which to truncate the SVD, or the regu-

larization parameter ϵ , can be chosen automatically using a method such as the L-curve, or in order to maximize the subjective quality of the image, as was done here.

The Hessian was calculated for the example above using one, two, and four wavelengths. Figure 7 shows the singular value spectra for these Hessians. The effect of Tikhonov regularization on the spectrum is also shown. First, it is clear that in the single wavelength case the condition number is huge, $\approx 10^{23}$, and so the single-wavelength Hessian is very ill-conditioned—evidence of the absorption-scattering nonuniqueness. Increasing the number of wavelengths in the Hessian from one to two improves the conditioning considerably, to perhaps 10^{11} . Interestingly, further increases in the number of wavelengths do not improve the conditioning more.

Intuitively, if the number of (independent) measurement samples, here $L \times M$, is greater than the number of unknown parameters, $(K+1) \times N$, then there is a good chance the nonuniqueness in the inversion will be overcome. Here, the inversion is for two parameters, and the significant reduction in the condition number of the Hessian when two wavelengths are included is indicative of this removal of the nonuniqueness.

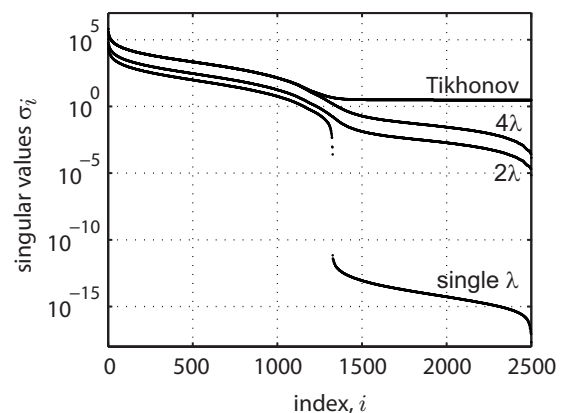


Fig. 7. Singular value spectrum of the Hessian matrix when data at one, two, and four wavelengths are used in its construction. The nonuniqueness in the single wavelength case gives rise to a gap in the singular value spectrum of several orders of magnitude. The nonuniqueness, and therefore the gap in the spectrum, disappears when two or more wavelengths are used in the reconstruction. However, the condition number is still large due to a second type of ill-posedness caused by the diffusive nature of the light propagation. This can be treated using standard techniques such as Tikhonov regularization, as shown.

Table 1. Ranges of the Absorption and Reduced Scattering Coefficients Used in the Multiwavelength Inversion Example as a Function of Wavelength

λ (nm)	μ_a (mm ⁻¹)	μ'_s (mm ⁻¹)
650	0.01–0.02	0.5–1.1
750	0.01–0.03	0.4–0.9
850	0.02–0.06	0.4–0.8
950	0.02–0.07	0.3–0.7

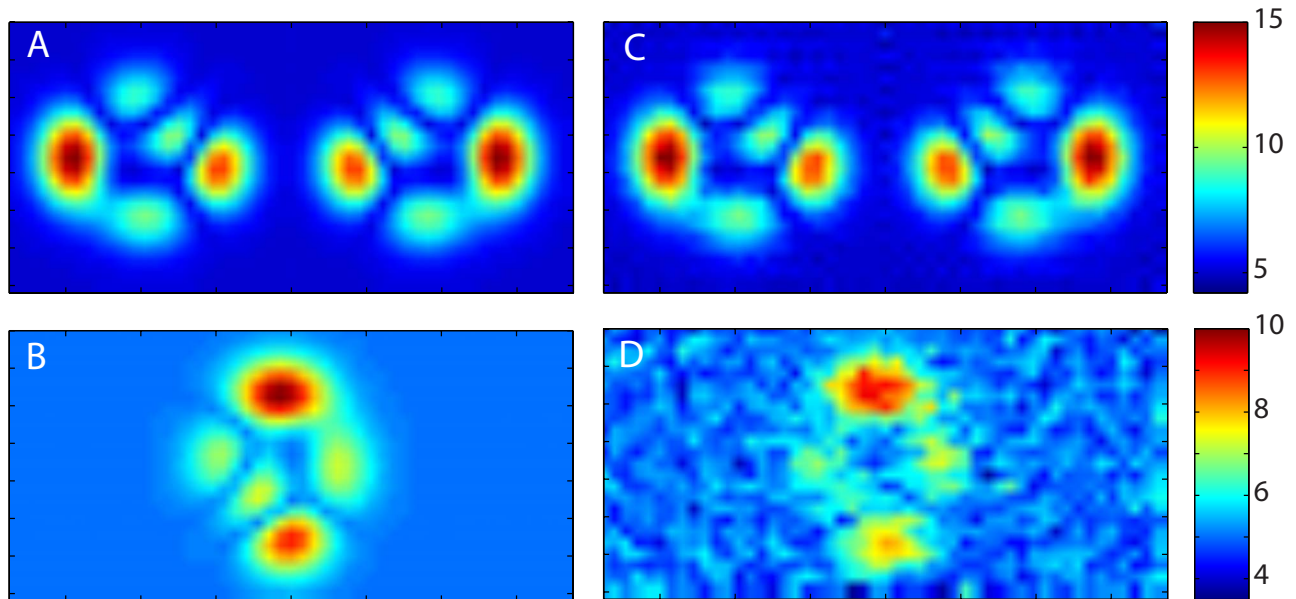


Fig. 8. (Color online) Results from Newton inversion using three iterations with Tikhonov regularization. (A) True chromophore concentration distribution $c(x)$ in (g/l). (B) True scattering distribution $a(x)$. (C) Recovered chromophore concentration estimate. (D) Recovered scattering distribution estimate. The initial distributions were chosen to be uniform and equal to 5 for both the chromophore concentration and the scattering. The image dimensions are 3.6 mm \times 7.5 mm. Profiles through these images are shown in Fig. 9. Both distributions have been recovered, without crosstalk between them, although the scattering is clearly more sensitive to the noise in this example.

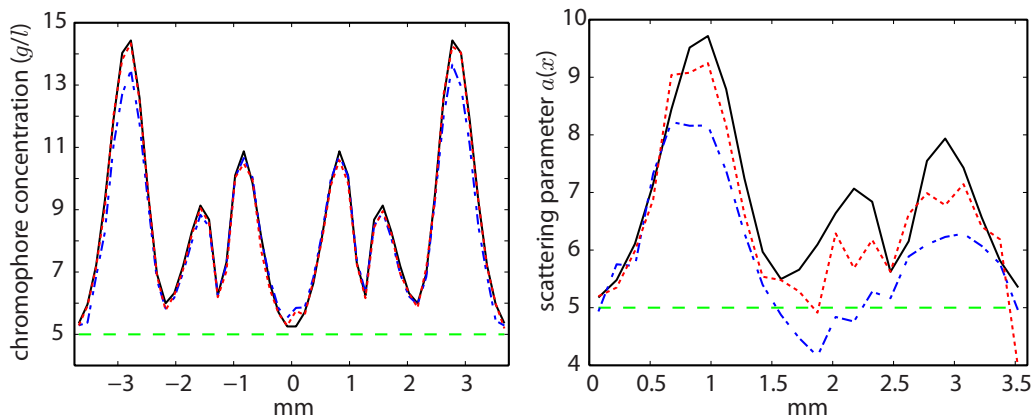


Fig. 9. (Color online) Profiles for the multiwavelength inversion example described in Subsection 4.E and Fig. 8. A central horizontal profile through the concentration distribution, and a central vertical profile through the scattering distribution show the true values (solid), initial guess (dashed), estimate after one Newton iteration (dotted-dashed) and after three iterations (dotted). The latter correspond to slices through Figs. 8C and 8D.

However, because of the diffusive nature of light transport in scattering media, and the subsequent blurring of high-spatial-frequency information, there remains a second type of ill-posedness, indicated by the gradual decay of the singular values. This type of ill-posedness is much less severe than the nonuniqueness and can be overcome by applying Tikhonov (or other) regularization.

The results of the inversion for $c(x)$ and $a(x)$, with an initial guess of 5 everywhere for both parameters, using data at four wavelengths, and following three Newton iterations with Tikhonov regularization are shown in Fig. 8. Profiles are shown in Fig. 9. Although the noise has affected the estimate of a more than that for c , it is clear that both parameters have successfully been recovered without any “crosstalk” between them.

5. DISCUSSION

In this paper, several approximations have been used in order to find a way to extract chromophore concentrations from photoacoustic images. First, it was assumed that a PAT image gives a measurement of the absorbed energy density distribution $\hat{h}(x)$. This is true only if (a) the initial pressure distribution $p_0(x)$ has been recovered exactly, and (b) the Grüneisen parameter $\Gamma(x)$ is known. Neither of these conditions will be quite true in practice, although with the use of calibrated broadband ultrasound detectors, a complete set of acoustic pressure measurements on a surface surrounding p_0 , and an exact image reconstruction algorithm, a good quantitative estimate of $p_0(x)$ is possible.

Second, an approximate light model was used to model the light transport in the tissue. The diffusion approximation will be accurate for depths greater than $\approx 1/\mu'_s$ (≈ 0.5 – 1 mm in tissue), and if a more accurate model is required for shallower depths, either one of the higher-order P_n approximations to the radiative transport equation [28] or the delta-Eddington adjustment to the diffusion equation formulation [6,40,41] could be used.

Third, the simulations in this paper are in two dimensions in order to keep the number of unknown parameters low and therefore the inversion tractable. In reality, the light will propagate in three dimensions. However, solutions to the diffusion equation do not differ fundamentally between two and three dimensions, and so the inverse problem is expected to behave similarly in three dimensions. Even for the very simple 2D example given in Subsection 4.E, the multiwavelength Jacobian required almost 100 MB storage. Clearly for more realistic problems, in three dimensions and with more chromophores, the matrices could easily become very large indeed. A 1 cm^3 image at $100\text{ }\mu\text{m}$ resolution—achievable with current PAT technology—has 1×10^6 voxels. If four chromophores and scattering are included in the inversion, the Hessian will have 25×10^{12} elements, requiring hundreds of terabytes of storage. This is a large-scale inverse problem, and while Newton's method was used here to demonstrate the principle that knowledge of the wavelength-dependence of scatter can be used to overcome the nonuniqueness, for a large scale problem it would not be feasible to store the Hessian, let alone calculate its inverse. (This might be feasible up to a point with state-of-the-art high-performance computing, but such facilities are not universally available.) In this case alternative approaches must be used. One key step is the adjoint model, Eq. (14), that can be used to calculate the gradients efficiently, even for large-scale problems. If the gradients can be calculated, then conjugate-gradient or quasi-Newton methods such as BFGS could be used to tackle the inversion, which would obviate the need to calculate the Hessian matrix directly.

Another practical issue of interest is the range of signal-to-noise ratios over which this inversion will work. This is not investigated in this paper, but it seems likely that when the target tissue is illuminated from just one direction, there will be a trade-off between the depth to which this inversion is accurate and the degree of attenuation of the light (the magnitude of the absorption and scattering coefficients). In some circumstances it may be possible to design illumination geometries to mitigate this difficulty.

6. CONCLUSIONS

The nonlinear optical inversion of photoacoustic (PAT) images for chromophore concentrations and scattering coefficients was described, and a framework given for their solution. The principle contributions of this paper are (1) to show that different chromophores can be separated using a multiwavelength approach when the optical scattering is known (an adjoint model was provided for the efficient calculation of the functional gradients in this case), (2) to show that a scattering-absorption nonuniqueness

prevents inversions for the absorption coefficient from a single-wavelength photoacoustic image unless the scattering is known *a priori*, and (3) the demonstration that the use of prior knowledge of the wavelength dependence of the scattering is sufficient to overcome this nonuniqueness and allow the recovery of the concentration distributions of the constituent chromophores.

ACKNOWLEDGMENTS

The authors thank Jan Laufer for helpful discussions. This work was funded by the Engineering and Physical Sciences Research Council (UK) (EPSRC).

REFERENCES

1. R. A. Kruger, P. Liu, Y. R. Fang, and C. R. Appledorn, "Photoacoustic ultrasound (PAUS)-reconstruction tomography," *Med. Phys.* **22**, 1605–1609 (1995).
2. C. G. A. Hoelen, F. F. M. de Mul, R. Pongers, and A. Dekker, "Three-dimensional photoacoustic imaging of blood vessels in tissue," *Opt. Lett.* **23**, 648–650 (1998).
3. X. Wang, Y. Pang, G. Ku, X. Xie, G. Stoica, and L. V. Wang, "Noninvasive laser-induced photoacoustic tomography for structural and functional in vivo imaging of the brain," *Nat. Biotechnol.* **21**, 803–806 (2003).
4. M. Xu and L. V. Wang, "Photoacoustic imaging in biomedicine," *Rev. Sci. Instrum.* **77**, 041101 (2006).
5. E. Z. Zhang, J. G. Laufer, and P. C. Beard, "Backward-mode multiwavelength photoacoustic scanner using a planar Fabry-Perot polymer film ultrasound sensor for high-resolution three-dimensional imaging of biological tissues," *Appl. Opt.* **47**, 561–577 (2008).
6. J. G. Laufer, C. Elwell, D. Delpy, and P. Beard, "In vitro measurements of absolute blood oxygen saturation using pulsed near-infrared photoacoustic spectroscopy: accuracy and resolution," *Phys. Med. Biol.* **50**, 4409–4428 (2005).
7. J. G. Laufer, C. Elwell, D. Delpy, and P. Beard, "Quantitative spatially resolved measurement of tissue chromophore concentrations using photoacoustic spectroscopy: application to the measurement of blood oxygenation and haemoglobin concentration," *Phys. Med. Biol.* **52**, 141–168 (2007).
8. M.-L. Li, J.-T. Oh, X. Xie, G. Ku, W. Wang, C. Li, G. Lungu, G. Stoica, and L. V. Wang, "Simultaneous molecular and hypoxia imaging of brain tumours in vivo using spectroscopic photoacoustic tomography," *Proc. IEEE* **96**, 481–489 (2008).
9. B. T. Cox, S. Arridge, K. Köstli, and P. Beard, "Quantitative photoacoustic imaging: fitting a model of light transport to the initial pressure distribution," *Proc. SPIE* **5697**, 49–55 (2005).
10. B. T. Cox, S. R. Arridge, K. Köstli, and P. C. Beard, "2D quantitative photoacoustic image reconstruction of absorption distributions in scattering media using a simple iterative method," *Appl. Opt.* **45**, 1866–1874 (2006).
11. K. Maslov, M. Sivaramakrishnan, H. F. Zhang, G. Stoica, and L. V. Wang, "Technical considerations in quantitative blood oxygenation measurement using photoacoustic microscopy in vivo," *Proc. SPIE* **6086**, 60860R (2006).
12. K. M. Stantz, B. Liu, M. Cao, D. Reinecke, K. Miller, and R. Kruger, "Photoacoustic spectroscopic imaging of intratumour heterogeneity and molecular identification," *Proc. SPIE* **6086**, 608605 (2006).
13. X. Wang, X. Xie, G. Ku, and L. V. Wang, "Noninvasive imaging of hemoglobin concentration and oxygenation in the rat brain using high-resolution photoacoustic imaging," *J. Biomed. Opt.* **11**, 024015 (2006).
14. K. Maslov, H. F. Zhang, and L. V. Wang, "Effects of wavelength-dependent fluence attenuation on the noninvasive photoacoustic imaging of hemoglobin oxygen

- saturation in subcutaneous vasculature *in vivo*,” *Inverse Probl.* **23**, S113–S122 (2007).
15. M. Sivaramakrishnan, K. Maslov, H. F. Zhang, G. Stoica, and L. V. Wang, “Limitations of quantitative photoacoustic measurements of blood oxygenation in small vessels,” *Phys. Med. Biol.* **52**, 1349–1361 (2008).
 16. A. de la Zerda, C. Zavaleta, S. Kere, S. Vaithilingam, S. Bodapati, Z. Liu, J. Levi, B. R. Smith, T.-J. Ma, O. Oralkan, Z. Cheng, X. Chen, H. Dai, B. T. Khuri-Yakub, and S. S. Gambhir, “Carbon nanotubes as photoacoustic molecular imaging agents in living mice,” *Nat. Nanotechnol.* **3**, 557–561 (2008).
 17. B. T. Cox, S. R. Arridge, and P. C. Beard, “Simultaneous estimation of chromophore concentration and scattering distributions from multiwavelength photoacoustic images,” *Proc. SPIE* **6856**, 68560Y (2008).
 18. B. T. Cox, S. Kara, S. R. Arridge, and P. C. Beard, “K-space propagation models for acoustically heterogeneous media: application to biomedical photoacoustics,” *J. Acoust. Soc. Am.* **121**, 3453–3464 (2007).
 19. B. T. Cox and P. C. Beard, “Fast calculation of pulsed photoacoustic fields in fluids using k-space methods,” *J. Acoust. Soc. Am.* **117**, 3616–3627 (2005).
 20. M. Agranovsky, P. Kuchment, and L. Kunyansky, “On reconstruction formulas and algorithms for thermoacoustic and photoacoustic tomography,” arXiv:0706.1303v1 (2007).
 21. A. Corlu, R. Choe, T. Durduran, K. Lee, M. Schweiger, S. Arridge, E. Hillman, and A. Yodh, “Diffuse optical tomography with spectral constraints and wavelength optimization,” *Appl. Opt.* **44**, 2082–2093 (2005).
 22. A. J. Welch and M. van Gemert, *Optical-Thermal Response of Laser-Irradiated Tissue* (Plenum, 1995).
 23. T. L. Troy and S. N. Thenadil, “Optical properties of human skin in the near infrared wavelength range of 1000 to 2200 nm,” *J. Biomed. Opt.* **6**, 167–176 (2001).
 24. A. N. Bashkatov, E. A. Genina, V. I. Kochubey, and V. V. Tuchin, “Optical properties of human skin, subcutaneous and mucous tissues in the wavelength range from 400 to 2000 nm,” *J. Phys. D: Appl. Phys.* **38**, 2543–2555 (2005).
 25. S.-H. Tseng, A. Grant, and A. J. Durkin, “In vivo determination of skin near-infrared optical properties using diffuse optical spectroscopy,” *J. Biomed. Opt.* **13**, 014016 (2008).
 26. S. L. Jacques and L. Wang, “Monte Carlo Modeling of Light Transport in Tissues,” in *Optical-Thermal Response of Laser-Irradiated Tissue*, A. J. Welch and M. J. C. Van Gemert, eds. (Plenum 1995).
 27. L. Wang, S. L. Jacques, and L. Zheng, “MCML -Monte Carlo modeling of light transport in multi-layered tissues,” *Comput. Methods Programs Biomed.* **47**, 131–146 (1995).
 28. S. R. Arridge, “Optical tomography in medical imaging,” *Inverse Probl.* **15**, R41–R93 (1999).
 29. S. Arridge, M. Schweiger, M. Hiraoka, and D. Delpy, “A finite element approach for modelling photon transport in tissue,” *Med. Phys.* **20**, 299–309 (1993).
 30. M. Schweiger, S. Arridge, M. Hiraoka, and D. Delpy, “The finite element method for the propagation of light in scattering media: Boundary and source conditions,” *Med. Phys.* **22**, 1779–1792 (1995).
 31. Z. Yuan and H. Jiang, “Quantitative photoacoustic tomography: Recovery of optical absorption coefficient maps of heterogeneous media,” *Appl. Phys. Lett.* **88**, 231101 (2006).
 32. B. Banerjee, S. Bagchi, R. M. Vasu, and D. Roy, “Quantitative photoacoustic tomography from boundary pressure measurements: noniterative recovery of optical absorption coefficient from the reconstructed absorbed energy map,” *J. Opt. Soc. Am. A* **25**, 2347–2356 (2008).
 33. J. Ripoll and V. Ntziachristos, “Quantitative point source photoacoustic inversion formulas for scattering and absorbing media,” *Phys. Rev. E* **71**, 031912 (2005).
 34. L. Yin, Q. Wang, Q. Zhang, and H. Jiang, “Tomographic imaging of absolute optical absorption coefficient in turbid media using combined photoacoustic and diffusing light measurements,” *Opt. Lett.* **32**, 2556–2558 (2007).
 35. Z. Yuan, Q. Wang, and H. Jiang, “Reconstruction of optical absorption coefficient maps of heterogeneous media by photoacoustic tomography coupled with diffusion equation based regularized Newton method,” *Opt. Express* **15**, 18076–18081 (2007).
 36. B. T. Cox, S. R. Arridge, and P. C. Beard, “Gradient-based quantitative photoacoustic image reconstruction for molecular imaging,” *Proc. SPIE* **6437**, 64371T (2007).
 37. W. H. Press, S. A. Teukolsky, W. T. Vetterling, and B. P. Flannery, *Numerical Recipes in C++, The Art of Scientific Computing* (Cambridge U. Press, 2005).
 38. L. N. Trefethen and D. Bau, *Numerical Linear Algebra* (SIAM, 1997).
 39. P. C. Hansen, “Deconvolution and regularization with Toeplitz matrices,” *Numer. Algorithms* **29**, 323–378 (2002).
 40. T. Spott and L. O. Svaasand, “Collimated light sources in the diffusion approximation,” *Appl. Opt.* **39**, 6453–6465 (2000).
 41. B. T. Cox, S. R. Arridge, and P. C. Beard, “Quantitative photoacoustic image reconstruction for molecular imaging,” *Proc. SPIE* **6086**, 60861M (2006).